



# High-Order Numerical Simulation of Flows over Rotating Cylinders of Various Cross-Sectional Shapes

Bin Zhang\* and Chunlei Liang†

*The George Washington University, Washington, DC 20052, USA*

2D and 3D flows over counterclockwise rotating cylinders of various cross-sectional shapes at  $Re = 200$  and  $1000$  and rotation ratio  $\alpha = \pi/4$  are numerically studied using a newly developed high-order sliding mesh method. It is found that all cylinders experience positive drag and negative lift throughout each rotating period. The circular cylinder has the largest mean forces at  $Re = 200$ . In contrast, the elliptic cylinder has the largest mean forces at  $Re = 1000$ . It is also noticed that, as the number of edges increases, the rotation frequency becomes less dominant in the flows, and the unsteady force amplitudes decrease. At  $Re = 1000$ , the 2D simulations over-predict forces for all cylinders except the elliptic one. Among all the flows, only that about the circular cylinder at  $Re = 200$  is found to be periodic. The flow around the elliptic cylinder exhibits two stable states at  $Re = 200$  and dramatically different flow structures from others at  $Re = 1000$ .

## I. Introduction

FLOW over cylinders has been an active research topic in fluid dynamics for almost a century. This problem involves simple geometries, yet is rich in physics, and is of great importance to the understanding of a wide range of flow problems. Examples include vortex dynamics, flow instability, unsteady hydrodynamic forces, heat transfer, acoustics, to name just a few. Zdravkovich's books [1, 2] provide a comprehensive review of previous research works on flow about circular cylinders, in which the flow is classified into several regimes based on the Reynolds number  $Re$ . For instance, creeping laminar flow when  $0 < Re < 4$ , separated laminar flow when  $4 < Re < 48$ , periodic vortex-shedding laminar flow when  $48 < Re < 180$ , and three-dimensional transitional flow when  $180 < Re < 400$ , etc.

But these classifications only apply to stationary cylinders. In fact, as Zdravkovich's books reflect, a majority of previous research works are about stationary cylinders. Rotating cylinders on the other hand, are less widely studied although they exist broadly in engineering applications. For example, they exist in a lot of transmitting mechanisms immersed in fluids, such as components of propellers, motors, drilling platforms, etc. They can also serve as ideal model problems for understanding flow about more complex rotating geometries.

Flow about rotating cylinders may or may not share similarities with flow about stationary cylinders depending on the rotation speed and the Reynolds number. Matsui [3] observed from experiments that when a circular cylinder rotates at a moderate speed, Karman vortex street, Gortler-type vortices and Taylor vortices are simultaneously generated in the flow field. Coutanceau and Menard [4] noticed that when rotation reaches a critical speed, the Karmam vortex street is completely suppressed. Chew et al. [5] confirmed this observation in their numerical study, and pointed out that lift and drag coefficients also approach asymptotic values when rotation speed is above critical. Mittal and Kumar [6] performed a series numerical simulation of a rotating circular cylinder at  $Re = 200$  with a wide range of rotation speed, and observed a second region of instability with one-sided vortex shedding. Chan et al. [7] studied a pair of side-by-side counter rotating circular cylinders numerically and experimentally. They noticed that a virtual elliptic body is formed and vortex shedding is suppressed when the cylinders are separated by certain distances and rotate above critical speeds.

\*Postdoctoral Scientist in the Department of Mechanical and Aerospace Engineering, email: bzh@gwu.edu

†Associate Professor in the Department of Mechanical and Aerospace Engineering, AIAA Associate Fellow

In this work, we are interested in the effects of geometric shape and Reynolds number on the fundamental properties (such as flow structures, unsteady forces, frequency distribution, etc.) of flow around rotating 2D and 3D cylinders. To deliver very high fidelity results, we employ our newly developed high-order sliding-mesh method [8–11] for the simulation. This method is designed for the spectral difference (SD) method [12–17] and the flux reconstruction (FR) method [18–24] on nonconforming sliding meshes. In this method, a computational domain is decomposed into non-overlapping subdomains that could rotate/slide with respect to the neighboring subdomains. A curved dynamic mortar element method [8–11] is proposed for communication between subdomains. In this way, the high-order accuracy and the conservation properties of the SD and the FR methods are retained on nonconforming unstructured dynamic grids. This method is ideal for simulating flow about rotating geometries in both 2D and 3D.

This paper is organized as follows. In Section II, we briefly introduce the governing equations and the numerical methods for solving them. Section III describes the details of the simulation set up. Simulation results are reported in Section IV. Finally, Section V concludes this paper.

## II. Numerical Methods

This section gives a brief description of the flow equations and the numerical methods for solving them on unstructured sliding mesh. More detailed information can be found in our previous papers [8–11].

### II.A. Governing Equations

We solve both the 2D and the 3D Navier-Stokes equations. For conciseness, we only discuss the 3D equations here, while the 2D equations are readily obtainable from the 3D equations. The conservative form of the 3D Navier-Stokes equations is

$$\frac{\partial \mathbf{Q}}{\partial t} + \frac{\partial \mathbf{F}}{\partial x} + \frac{\partial \mathbf{G}}{\partial y} + \frac{\partial \mathbf{H}}{\partial z} = 0, \quad (1)$$

where  $\mathbf{Q}$ ,  $\mathbf{F}$ ,  $\mathbf{G}$ ,  $\mathbf{H}$  are the vectors of conservative variables and fluxes, respectively. More specifically,

$$\mathbf{Q} = [\rho \ \rho u \ \rho v \ \rho w \ E]^\top, \quad (2)$$

$$\mathbf{F} = \mathbf{F}_{inv}(\mathbf{Q}) + \mathbf{F}_{vis}(\mathbf{Q}, \nabla \mathbf{Q}), \quad (3)$$

$$\mathbf{G} = \mathbf{G}_{inv}(\mathbf{Q}) + \mathbf{G}_{vis}(\mathbf{Q}, \nabla \mathbf{Q}), \quad (4)$$

$$\mathbf{H} = \mathbf{H}_{inv}(\mathbf{Q}) + \mathbf{H}_{vis}(\mathbf{Q}, \nabla \mathbf{Q}), \quad (5)$$

where  $\rho$  is density,  $u$ ,  $v$  and  $w$  are the velocity components,  $E$  is the total energy per volume defined as

$$E = \frac{p}{\gamma - 1} + \frac{1}{2}\rho(u^2 + v^2 + w^2), \quad (6)$$

and  $p$  is pressure,  $\gamma$  is the ratio of specific heats and is set to 1.4 in the present work. The inviscid flux vectors are

$$\mathbf{F}_{inv} = \begin{bmatrix} \rho u \\ \rho u^2 + p \\ \rho uv \\ \rho uw \\ (E + p)u \end{bmatrix}, \quad \mathbf{G}_{inv} = \begin{bmatrix} \rho v \\ \rho uv \\ \rho v^2 + p \\ \rho vw \\ (E + p)v \end{bmatrix}, \quad \mathbf{H}_{inv} = \begin{bmatrix} \rho w \\ \rho vw \\ \rho w^2 + p \\ (E + p)w \end{bmatrix}. \quad (7)$$

The viscous flux vectors are

$$\mathbf{F}_{vis} = - \begin{bmatrix} 0 \\ \tau_{xx} \\ \tau_{yx} \\ \tau_{zx} \\ u\tau_{xx} + v\tau_{yx} + w\tau_{zx} + kT_x \end{bmatrix}, \quad (8)$$

$$\mathbf{G}_{vis} = - \begin{bmatrix} 0 \\ \tau_{xy} \\ \tau_{yy} \\ \tau_{zy} \\ u\tau_{xy} + v\tau_{yy} + w\tau_{zy} + kT_y \end{bmatrix}, \quad \mathbf{H}_{vis} = - \begin{bmatrix} 0 \\ \tau_{xz} \\ \tau_{yz} \\ \tau_{zz} \\ u\tau_{xz} + v\tau_{yz} + w\tau_{zz} + kT_z \end{bmatrix}, \quad (9)$$

where  $\tau_{ij} = \mu(u_{i,j} + u_{j,i}) + \lambda\delta_{ij}u_{k,k}$  is the shear stress tensor,  $\mu$  is the dynamic viscosity,  $\lambda = -2/3\mu$  based on the Stokes' hypothesis,  $\delta_{ij}$  is the Kronecker delta,  $k$  is the thermal conductivity,  $T$  is temperature which is related to density and pressure through the ideal gas law  $p = \rho RT$ , and  $R$  is the gas constant.

## II.B. Computational Equations

To simulate flow on moving grids, we transform the Navier-Stokes equations to the following computational form using the arbitrary Lagrangian-Eulerian (ALE) approach,

$$\frac{\partial \tilde{\mathbf{Q}}}{\partial t} + \frac{\partial \tilde{\mathbf{F}}}{\partial \xi} + \frac{\partial \tilde{\mathbf{G}}}{\partial \eta} + \frac{\partial \tilde{\mathbf{H}}}{\partial \zeta} = 0, \quad (10)$$

where  $(\xi, \eta, \zeta)$  are the computational coordinates,  $\tilde{\mathbf{Q}}$  is the computational solution vector,  $\tilde{\mathbf{F}}$ ,  $\tilde{\mathbf{G}}$  and  $\tilde{\mathbf{H}}$  are the computational flux vectors. These terms are related to the physical ones through

$$\begin{pmatrix} \tilde{\mathbf{Q}} \\ \tilde{\mathbf{F}} \\ \tilde{\mathbf{G}} \\ \tilde{\mathbf{H}} \end{pmatrix} = |\mathcal{J}| \mathcal{J}^{-1} \begin{pmatrix} \mathbf{Q} \\ \mathbf{F} \\ \mathbf{G} \\ \mathbf{H} \end{pmatrix}, \quad (11)$$

where  $|\mathcal{J}|$  is the determinant of the Jacobian matrix, and  $\mathcal{J}^{-1}$  is the inverse Jacobian matrix. Their expressions are

$$\mathcal{J} = \frac{\partial(t, x, y, z)}{\partial(t, \xi, \eta, \zeta)} = \begin{bmatrix} 1 & 0 & 0 & 0 \\ x_t & x_\xi & x_\eta & x_\zeta \\ y_t & y_\xi & y_\eta & y_\zeta \\ z_t & z_\xi & z_\eta & z_\zeta \end{bmatrix}, \quad (12)$$

$$\mathcal{J}^{-1} = \frac{\partial(t, \xi, \eta, \zeta)}{\partial(t, x, y, z)} = \begin{bmatrix} 1 & 0 & 0 & 0 \\ \xi_t & \xi_x & \xi_y & \xi_z \\ \eta_t & \eta_x & \eta_y & \eta_z \\ \zeta_t & \zeta_x & \zeta_y & \zeta_z \end{bmatrix}. \quad (13)$$

To ensure free-stream preservation on moving grids, the following geometric conservation laws (GCL) [25] must also be satisfied numerically,

$$\begin{cases} \frac{\partial}{\partial \xi} (|\mathcal{J}| \xi_x) + \frac{\partial}{\partial \eta} (|\mathcal{J}| \eta_x) + \frac{\partial}{\partial \zeta} (|\mathcal{J}| \zeta_x) = 0, & (14) \end{cases}$$

$$\begin{cases} \frac{\partial}{\partial \xi} (|\mathcal{J}| \xi_y) + \frac{\partial}{\partial \eta} (|\mathcal{J}| \eta_y) + \frac{\partial}{\partial \zeta} (|\mathcal{J}| \zeta_y) = 0, & (15) \end{cases}$$

$$\begin{cases} \frac{\partial}{\partial \xi} (|\mathcal{J}| \xi_z) + \frac{\partial}{\partial \eta} (|\mathcal{J}| \eta_z) + \frac{\partial}{\partial \zeta} (|\mathcal{J}| \zeta_z) = 0, & (16) \end{cases}$$

$$\begin{cases} \frac{\partial |\mathcal{J}|}{\partial t} + \frac{\partial}{\partial \xi} (|\mathcal{J}| \xi_t) + \frac{\partial}{\partial \eta} (|\mathcal{J}| \eta_t) + \frac{\partial}{\partial \zeta} (|\mathcal{J}| \zeta_t) = 0. & (17) \end{cases}$$

In this work, grid motion is analytically controlled, and the spatial discretization is direct differentiation (will be discussed later), the first three GCL equations are therefore automatically satisfied. From the last equation,  $|\mathcal{J}|$  is treated as an unknown, and is solved for using the same temporal and spatial discretization methods as for the flow equations. This numerical  $|\mathcal{J}|$  is then used to update the physical solutions.

### II.C. Flux Reconstruction Method

In flux reconstruction (FR) method, each grid element is mapped to a standard computational element (unit square in 2D, unit cube in 3D) using the iso-parametric mapping. Solution points (SPs) and flux points (FPs) are then defined in the interior and on the boundaries, respectively, of a standard element. For an  $N$ -th order FR method,  $N$  SPs are defined in each coordinate direction, and  $N$  FPs are defined along each direction of a boundary face. Fig. 1 shows a 2D view of the SPs and FPs for a fourth-order FR scheme. Let

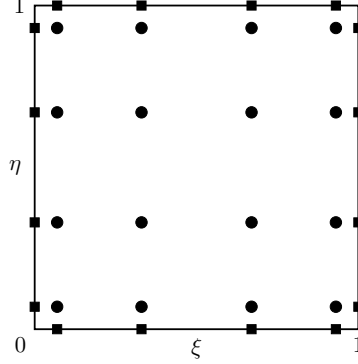


Figure 1. 2D view of solution points (circular dots) and flux points (square dots) for a fourth-order FR scheme.

$X_s$  denote the coordinate of an SP, we define the following Lagrange interpolation basis at the  $i$ -th SP,

$$h_i(X) = \prod_{s=1, s \neq i}^N \left( \frac{X - X_s}{X_i - X_s} \right). \quad (18)$$

This allows the construction of solution and flux polynomials by tensor products of the interpolation bases:

$$\tilde{\mathbf{Q}}(\xi, \eta, \zeta) = \sum_{k=1}^N \sum_{j=1}^N \sum_{i=1}^N \tilde{\mathbf{Q}}_{ijk} h_i(\xi) h_j(\eta) h_k(\zeta), \quad (19)$$

$$\tilde{\mathbf{F}}(\xi, \eta, \zeta) = \sum_{k=1}^N \sum_{j=1}^N \sum_{i=1}^N \tilde{\mathbf{F}}_{ijk} h_i(\xi) h_j(\eta) h_k(\zeta), \quad (20)$$

$$\tilde{\mathbf{G}}(\xi, \eta, \zeta) = \sum_{k=1}^N \sum_{j=1}^N \sum_{i=1}^N \tilde{\mathbf{G}}_{ijk} h_i(\xi) h_j(\eta) h_k(\zeta), \quad (21)$$

$$\tilde{\mathbf{H}}(\xi, \eta, \zeta) = \sum_{k=1}^N \sum_{j=1}^N \sum_{i=1}^N \tilde{\mathbf{H}}_{ijk} h_i(\xi) h_j(\eta) h_k(\zeta), \quad (22)$$

where  $\tilde{\mathbf{Q}}_{ijk}$ ,  $\tilde{\mathbf{F}}_{ijk}$ ,  $\tilde{\mathbf{G}}_{ijk}$  and  $\tilde{\mathbf{H}}_{ijk}$  are the computational variable and fluxes at the  $(i, j, k)$ -th SP.

These polynomials are only continuous within each element, but discontinuous across element boundaries. Therefore, common values need to be defined at cell boundaries. Here, the common solutions are calculated as the average of the left and the right values of a boundary. The common inviscid fluxes are computed using a Riemann solver, for example, the Rusanov solver [26]. The common viscous fluxes are computed from the common solution and common gradients, where the common gradients are also calculated as the average of the left and the right values of a boundary.

Meanwhile, due to the first-order spatial derivatives on fluxes in the governing equations, the flux polynomials need to be at least one degree higher than the solution polynomial to obtain the correct orders of accuracy. This is achieved by using correction functions. For example, flux in the  $\xi$  direction is corrected to

$$\tilde{\mathbf{F}}_c(\xi) = \tilde{\mathbf{F}}(\xi) + (\tilde{\mathbf{F}}_L^{com} - \tilde{\mathbf{F}}_L) \cdot g_L(\xi) + (\tilde{\mathbf{F}}_R^{com} - \tilde{\mathbf{F}}_R) \cdot g_R(\xi), \quad (23)$$

where  $\tilde{\mathbf{F}}_L^{com}$  and  $\tilde{\mathbf{F}}_L$  are the common and the discontinuous fluxes at  $\xi = 0$ , and  $\tilde{\mathbf{F}}_R^{com}$  and  $\tilde{\mathbf{F}}_R$  are the values at  $\xi = 1$ ,  $g_L(\xi)$  and  $g_R(\xi)$  are the left and the right correction functions. The correction functions are

polynomials that are at least one-degree higher than the original flux polynomials. They must satisfy

$$g_L(0) = 1, \quad g_L(1) = 0, \quad g_R(0) = 0, \quad g_R(1) = 1, \quad (24)$$

in order to ensure continuity. In this work, we use the  $g_{DG}$  correction function [18, 19] for this purpose.

Finally, the computational equation is written in the following residual form by moving the flux terms to the right hand side,

$$\frac{\partial \tilde{\mathbf{Q}}}{\partial t} = -\frac{\partial \tilde{\mathbf{F}}_c}{\partial \xi} - \frac{\partial \tilde{\mathbf{G}}_c}{\partial \eta} - \frac{\partial \tilde{\mathbf{H}}_c}{\partial \zeta}, \quad (25)$$

and it is then time marched using a five-stage fourth-order strong stability preserving Runge-Kutta (SSP-RK) method [27, 28] for all the simulations in this work.

## II.D. Sliding-Mesh Method

To simulate flow about rotating geometries, we split a computational domain into non-overlapping subdomains using sliding-mesh interfaces. Fig. 2 shows the simplest sliding meshes in 3D and 2D.

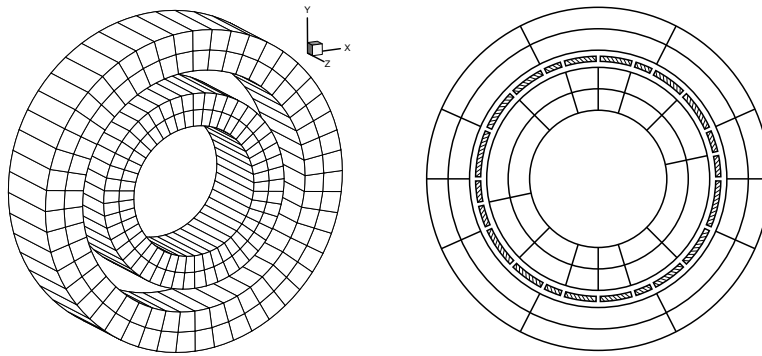


Figure 2. A 3D (left, inner domain is scaled) and a 2D (right) sliding meshes (hatched lines are mortar elements).

To deal with the nonconforming sliding-mesh interfaces, we developed a curved dynamic mortar method [8–10], and recently extended this method to nonuniform sliding meshes [11] and also to vortex-induced vibrations [29] with straight sliding interfaces. In this method, we first project the discontinuous solutions from the two sides of a sliding interface to mortar elements. Then, common solutions and common fluxes are computed on the mortars. Finally, we project these common values from mortars back to cell faces to ensure continuity and conservation. This method maintains the high-order spatial and temporal accuracies of the SD/FR method and the SSP-RK methods, and is very efficient in terms of computational cost.

## III. Simulation Setup

Cylinders with four different cross-sectional shapes are studied: elliptic (2 edges/corners), triangular (3 edges/corners), square (4 edges/corners), and circular ( $\infty$  edges/corners). The elliptic cylinder has a minor to major axis length ratio of 0.5. The triangular cylinder is equilateral. Before proceeding further, let us define radius and diameter of a cylinder. As shown in Fig. 3, the radius (denoted by  $R$ ) of a non-circular cylinder is defined as the distance from the center of the cylinder to any one of its vertices. The diameter (denoted by  $D$ ) is simply twice the radius, i.e.,  $D = 2R$ . For all the cylinders studied in this work, we have chosen  $R = 0.5$  (i.e.,  $D = 1.0$ ). Hereinafter, without further explanation, we use (a), (b), (c) and (d) to denote elliptic, triangular, square and circular cylinders, respectively.

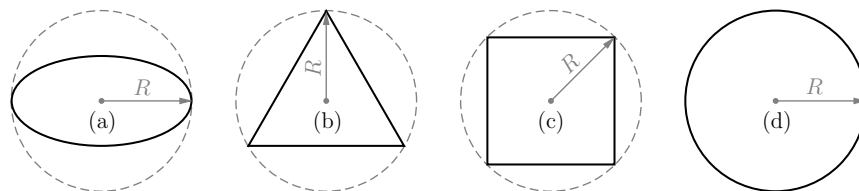


Figure 3. Definition of radius of cylinders with different cross-sectional shapes.

Meshes for the 2D cylinders are shown in Fig. 4. Each domain has an overall size of  $100 \times 100$ , and is split into an outer and an inner subdomain by a sliding interface whose radius is 0.8. All simulations have the same outer subdomain with 8,369 elements as shown on the left. The inner meshes are shown on the right, and they have 372/443/324/200 elements, respectively. Each cylinder locates  $30D$  away from the inlet and  $70D$  away from the outlet. It is worth noting that, meshes around all curved boundaries have high-order quadratic elements. The inlet is set as Dirichlet boundary. The top, the bottom and the outlet are treated as characteristic farfield boundaries. All cylinder surfaces are treated as no-slip adiabatic walls.

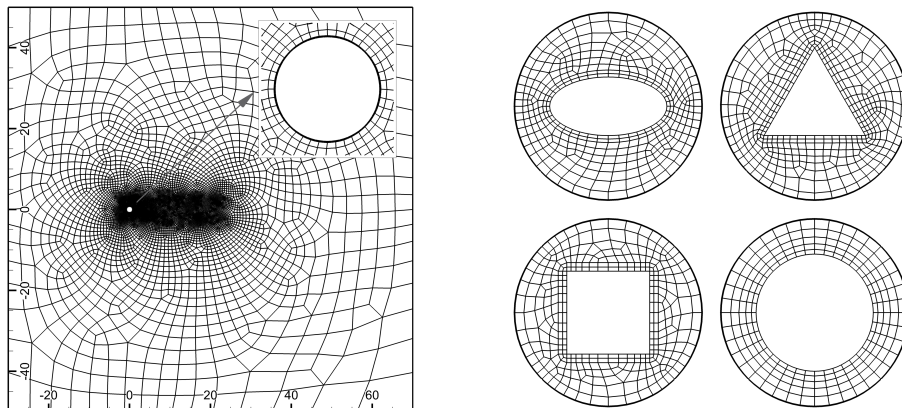


Figure 4. Meshes for the 2D rotating cylinders: left, outer mesh; right, inner rotating mesh around each cylinder.

Meshes for the 3D cylinders are shown in Fig. 5. They are obtained by extruding the 2D meshes in the spanwise (i.e.,  $z$ ) direction. The spanwise direction has a length of 5, and is uniformly meshes into 20 elements, resulting in a total number of about 170 thousand elements for each case. Lei et al. [30] studied the effects of spanwise length on the simulation of flow over cylinders. They found that when the length is above twice the cylinder diameter, the effects become minor. Therefore, we expect the present spanwise length not to have obvious effects on the simulation. Similar to the 2D simulations, the inlet is set as a Dirichlet boundary. The top, the bottom and the outlet are treated as characteristic farfield boundaries. The two spanwise boundaries are set as periodic. All cylinder surfaces are set as no-slip adiabatic walls.

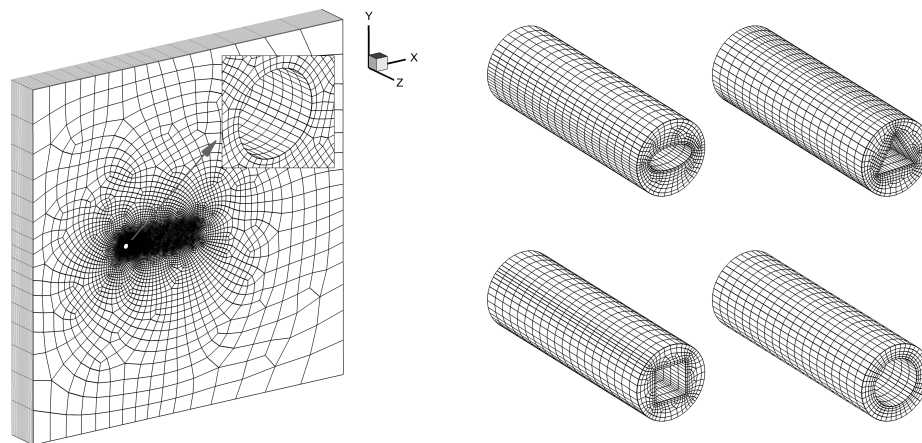


Figure 5. Meshes for the 3D rotating cylinders: left, outer mesh; right, inner rotating mesh around each cylinder.

For all the simulations, the incoming freestream flow has a Mach number  $Ma = 0.1$ . All cylinders rotate counterclockwise about the  $z$  axis at an angular speed  $\omega D/U_\infty = \pi/2$ , i.e., with a rotation period  $TU_\infty/D = 4$  and rotation frequency  $f_0 D/U_\infty = 0.25$ . This configuration gives a rotation ratio  $\alpha = \omega R/U_\infty = \pi/4$ . Two Reynolds numbers:  $Re = \rho_\infty U_\infty D/\mu_\infty = 200$  and 1000, are studied for all the cylinders. All simulations are started from the uniform free-stream flow and continued for  $tU_\infty/D = 400$  time units (i.e., 100 rotation periods) using the 6-th order sliding-mesh FR method and a fourth-order time-marching scheme (discussed in the previous section) with a time-step size  $\Delta t U_\infty/D = 2.0 \times 10^{-4}$ .

## IV. Simulation Results

In this section, we report simulation results on several fundamental properties of the flow, including flow forces, flow frequencies and flow field structures. Among them, the flow forces are measured by the lift coefficient  $C_L$  and the drag coefficient  $C_D$  that are defined as

$$C_L = Y / (\frac{1}{2} \rho_\infty U_\infty^2 D L_z), \quad (26)$$

$$C_D = X / (\frac{1}{2} \rho_\infty U_\infty^2 D L_z), \quad (27)$$

where  $Y$  and  $X$  are the lift and the drag forces exerted on a cylinder by the flow;  $\rho_\infty$  and  $U_\infty$  are free-stream fluid density and flow speed;  $D$  is the diameter of a cylinder;  $L_z$  is the spanwise length of a cylinder (taken as 1 for 2D cylinders). There are two sources for each force, one is pressure, the other is friction. For this reason, the lift and drag coefficients can be decomposed to

$$C_L = C_{L,p} + C_{L,f}, \quad C_D = C_{D,p} + C_{D,f}, \quad (28)$$

where the subscripts ‘ $p$ ’ and ‘ $f$ ’ denote ‘pressure’ and ‘friction’, respectively. Each coefficient can also be decomposed into steady and unsteady components, for example,

$$C_L = \bar{C}_L + c_L, \quad C_D = \bar{C}_D + c_D, \quad (29)$$

where

$$\bar{C}_L = \left. \frac{\int_{t_1}^{t_2} C_L dt}{t_2 - t_1} \right|_{(t_2-t_1) \rightarrow \infty} \quad \text{and} \quad \bar{C}_D = \left. \frac{\int_{t_1}^{t_2} C_D dt}{t_2 - t_1} \right|_{(t_2-t_1) \rightarrow \infty} \quad (30)$$

are the mean lift and drag coefficients;  $c_L$  and  $c_D$  are the unsteady lift and drag coefficients from which the spectra of the flow will be computed. Also of interests are the root-mean-square (rms) values of the unsteady components, for instance,

$$(c_L)_{rms} = \sqrt{\left. \frac{\int_{t_1}^{t_2} (c_L)^2 dt}{t_2 - t_1} \right|_{(t_2-t_1) \rightarrow \infty}} \quad \text{and} \quad (c_D)_{rms} = \sqrt{\left. \frac{\int_{t_1}^{t_2} (c_D)^2 dt}{t_2 - t_1} \right|_{(t_2-t_1) \rightarrow \infty}} \quad (31)$$

where  $(t_2 - t_1) \rightarrow \infty$  means that the integration must include data from long enough time.

### IV.A. Reynolds Number 200

At this Reynolds number, the 3D cases remain two-dimensional throughout the simulation, and no difference was observed from the 2D results. For this reason, we only report results from the 2D simulation.

#### IV.A.1. Flow Forces

For each cylinder, an overall view and a close view of the histories of the force coefficients are plotted in Fig. 6 and Fig. 7, respectively. Several observations can be made from these curves. Firstly, all the cylinders experience a positive drag and a negative lift all the time (Magnus effect). Secondly, in despite of different cross-sectional shapes, all the cylinders experience drags, and also lifts, of similar magnitudes. Thirdly, the oscillation amplitudes of the forces seem to decrease as the number of cylinder edges increases, especially for the drag coefficient. Last but not least, all curves show distinct characteristics on periodicity. For example, those of the elliptic cylinder are obviously not periodic (from the overall view), and those of the circular cylinder are very much periodic. Interestingly, it was reported in [31] that the flow over an elliptic cylinder (with the same configurations as in this work) is periodic. Their conclusion is probably due to the short simulation time, and thus does not provide a complete picture of the flow.

The mean force coefficients and the rms values (represent oscillation amplitudes) are reported in Table 1 and Table 2 for the lift and the drag, respectively. Data from  $tU_\infty/D = 100$  to 400, which covers 75 rotation periods, was used for the calculation. First of all, we see that the circular cylinder experiences the largest lift, while the other cylinder experience similar lifts; and all cylinders experience similar drags. Secondly, for all the cylinders, pressure is found to have dominant contribution to both the mean forces and the oscillations (as the pressure components are much larger than the friction components). Thirdly, friction has similar

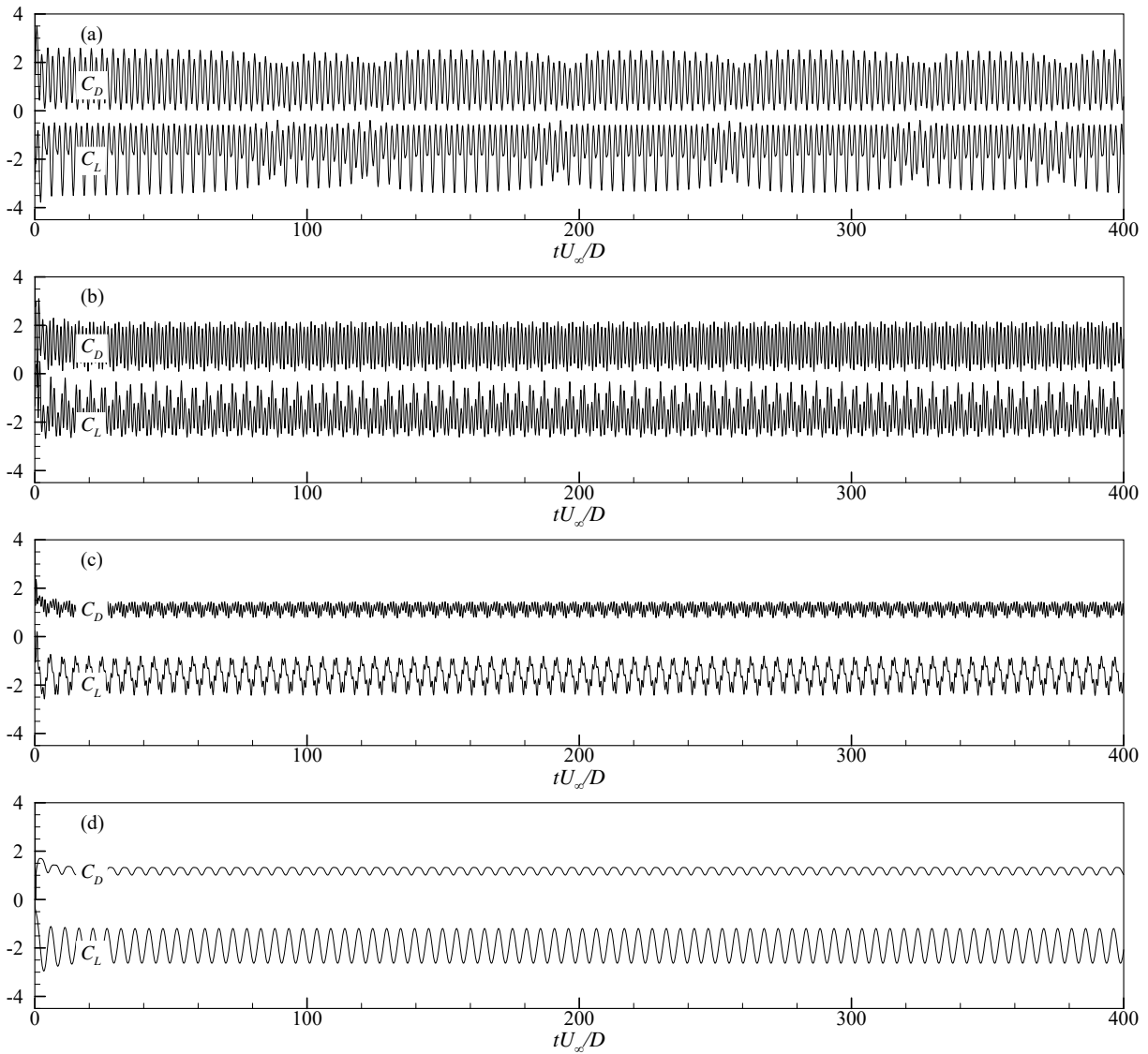


Figure 6. Overall views of the lift and drag coefficients at  $Re = 200$ .

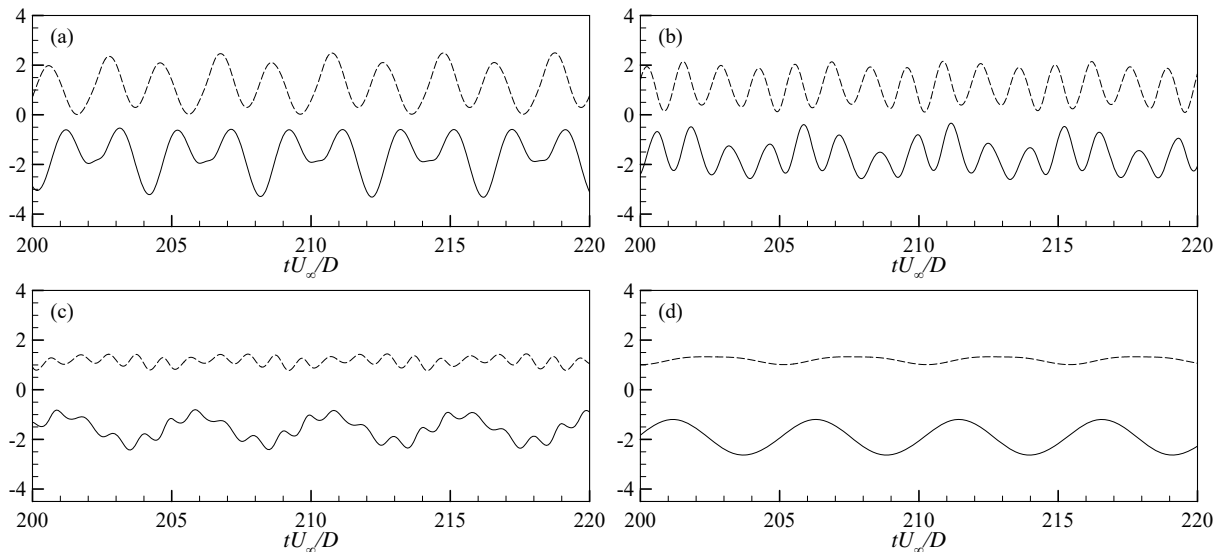


Figure 7. Close views of the lift (solid) and drag (dashed) coefficients at  $Re = 200$ .

contribution (in percentage) to the mean lift of all the cylinders. Fourthly, friction has more contribution (in percentage) to the mean drags of the elliptic and the circular cylinders than to the triangular and the square cylinders. This is probably because of the smooth surface of the elliptic and the circular cylinders, where the flows are more attached than those of the triangular and the square cylinders with sharp surfaces. Lastly, from  $(c_{L,f})_{rms}:(c_{L,p})_{rms}$  and  $(c_{D,f})_{rms}:(c_{D,p})_{rms}$ , we see that friction causes larger unsteady forces on the triangular and the square cylinders than on the elliptic and the circular cylinders.

	$\bar{C}_L$	$\bar{C}_{L,p}$	$\bar{C}_{L,f}$	$(c_L)_{rms}$	$(c_{L,p})_{rms}$	$(c_{L,f})_{rms}$	$(c_{L,f})_{rms}:(c_{L,p})_{rms}$
elliptic	-1.638	-1.538 (93.9%)	-0.099 (6.1%)	0.794	0.782	0.040	5.1:100
triangular	-1.659	-1.535 (92.5%)	-0.124 (7.5%)	0.594	0.651	0.093	14.3:100
square	-1.583	-1.484 (93.7%)	-0.099 (6.3%)	0.439	0.402	0.046	11.4:100
circular	-1.924	-1.834 (95.3%)	-0.090 (4.7%)	0.507	0.466	0.045	9.7:100

Table 1. Mean and rms values of the lift coefficients at  $Re = 200$ .

	$\bar{C}_D$	$\bar{C}_{D,p}$	$\bar{C}_{D,f}$	$(c_D)_{rms}$	$(c_{D,p})_{rms}$	$(c_{D,f})_{rms}$	$(c_{D,f})_{rms}:(c_{D,p})_{rms}$
elliptic	1.165	0.949 (81.5%)	0.216 (18.5%)	0.748	0.738	0.023	3.1:100
triangular	1.139	1.058 (92.9%)	0.081 ( 7.1%)	0.614	0.679	0.098	14.4:100
square	1.153	1.046 (90.7%)	0.107 ( 9.3%)	0.175	0.151	0.038	25.2:100
circular	1.202	0.947 (78.8%)	0.255 (21.2%)	0.114	0.116	0.012	10.3:100

Table 2. Mean and rms values of the drag coefficients at  $Re = 200$ .

The periodicities of the flows are more evident if we plot  $C_L$  and  $C_D$  in the phase diagram as shown in Fig. 8, where the data is from  $tU_\infty/D = 200$  to 300, i.e., 25 rotation periods. A curve in the phase diagram will perfectly repeat itself if the flow is perfectly periodic. Based on this information, we can confidently conclude that among the four cylinders, only the flow around the circular cylinder is perfectly periodic, while those around the other three cylinders are obviously not periodic.

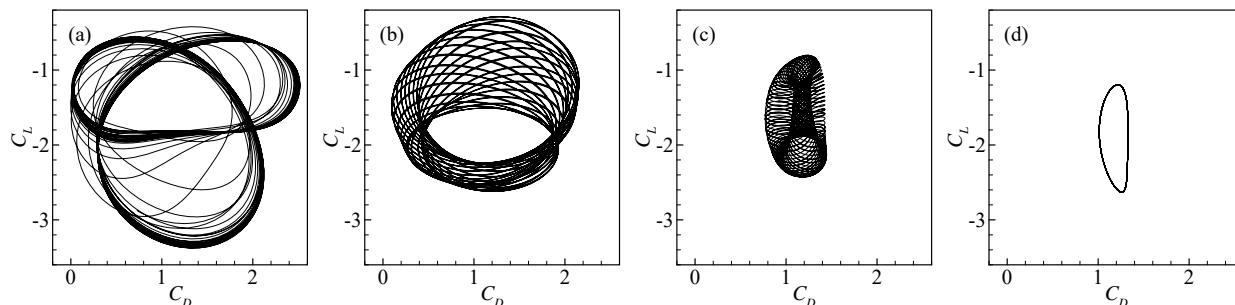


Figure 8. Phase diagrams of  $C_L$  and  $C_D$  for the cylinders at  $Re = 200$ .

#### IV.A.2. Flow Frequencies

To see the frequency distribution of the flows, we performed a fast Fourier transformation on the unsteady force coefficients. The resulting spectra are plotted in Fig. 9, and the dominant frequencies are summarized in Table 3. For the elliptic cylinder, the dominant frequencies on the unsteady lift and the unsteady drag are both found to be 0.50, which is twice the rotation frequency. This is because of the geometric symmetry (two corners) that introduces disturbances to the flow at twice the rotation frequency. Similarly, the dominant frequencies on  $c_L$  and  $c_D$  for the triangular cylinder are both found to be 0.75, which is three times the rotation frequency. This is again because of the geometric symmetry of this cylinder. However, for the square cylinder, the dominant frequency on  $c_L$  is 0.210, which is not a multiple of the rotation frequency. This trend continues to the circular cylinder, where both dominant frequencies on  $c_L$  and  $c_D$  are not multiples

of the rotation frequency. This is possibly because that, as the number of edges increases, the rotation motion introduces a more continuous (higher frequency) disturbance to the flow. And this higher-frequency disturbance triggers intrinsic frequencies of the flows.

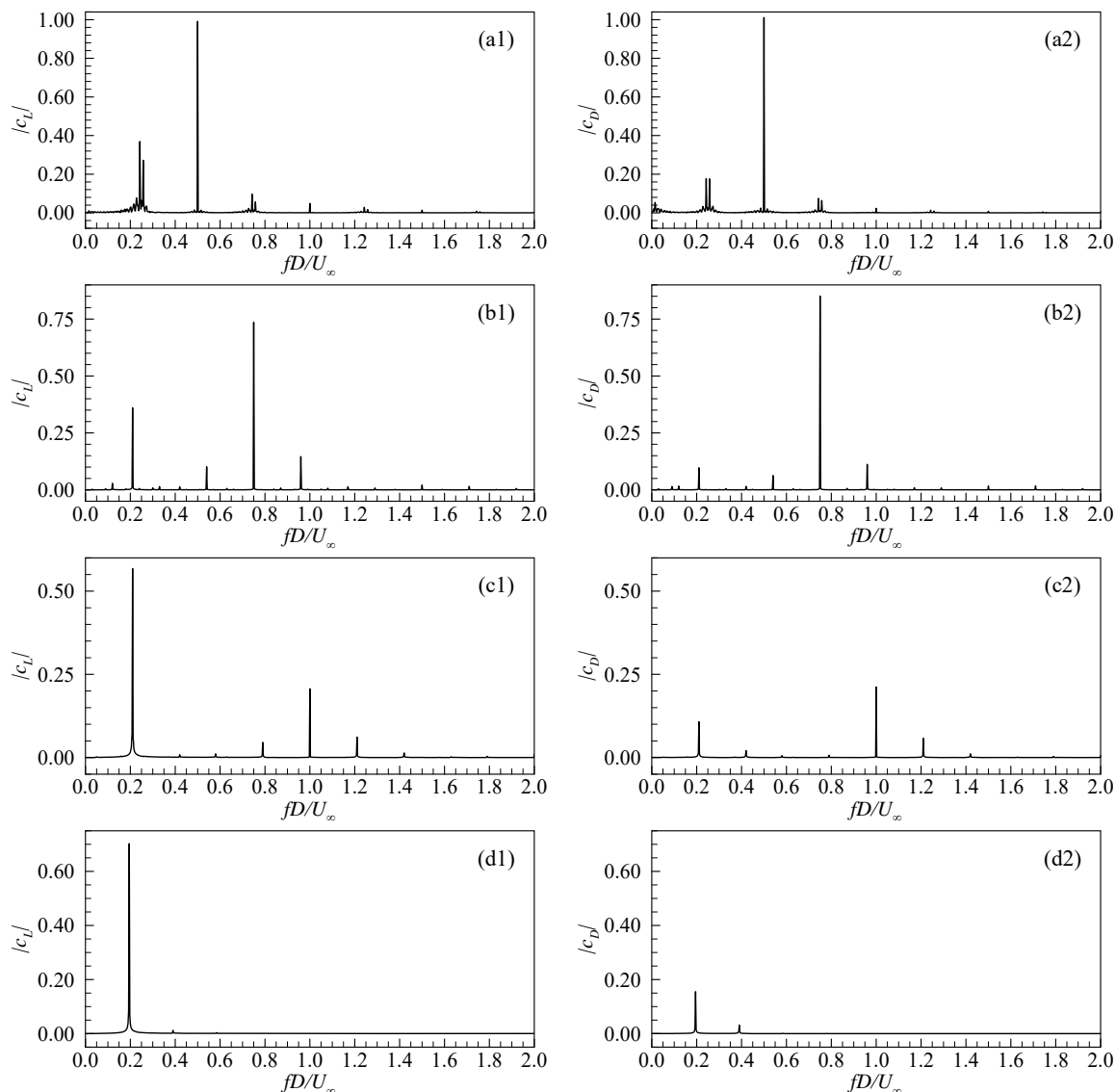


Figure 9. Spectra of the unsteady lift and drag coefficients at  $Re = 200$ .

	elliptic	triangular	square	circular
$f_L^*$	0.500	0.750	0.210	0.195
$f_D^*$	0.500	0.750	1.000	0.195

Table 3. Dominant frequencies on the unsteady lift and drag coefficients at  $Re = 200$ .

#### IV.A.3. Flow Fields

Fig. 10 shows instantaneous views of the flow fields. It is seen that the elliptical cylinder has a wake with two distinct rows: an upper row of negative vortices and a lower row of positive ones. In contrast, the other cylinders have very similar wakes with only a single row of alternative positive and negative vortices. It is also seen that the sharp corners of the triangular and the square cylinders generate multiple vortices in each

rotation period. And these vortices interact locally and also with vortices from the upper surface, which creates more unsteadiness to the flows and in turn on the forces.

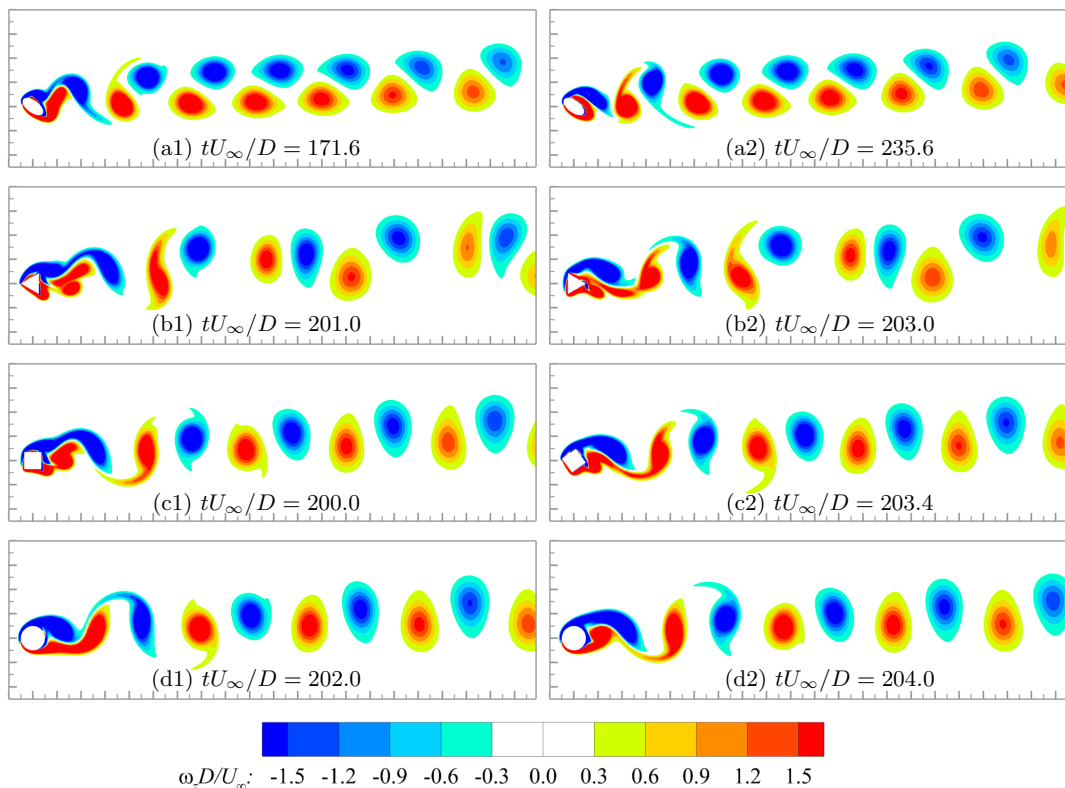


Figure 10. Typical instantaneous vorticity contours of flow over rotating cylinders at  $Re = 200$ .

One more interesting observation on the elliptic cylinder is that its  $C_D$  and  $C_L$  curves (see Fig. 6(a)) show a distinct pattern that those of the other cylinders do not: an envelope with alternative wide peaks (troughs for  $C_L$ ) separated by small dips. Through flow field visualization, it is found that these alternative peaks (troughs) actually represent two stable states of the flow, and the dips represent the transitional process between the two states. As an example, we plot in Fig. 11 (1) and (3) two instantaneous flow fields when the cylinder rotates to its initial position (i.e., at phase  $\phi = 0^\circ$ ) during the two stable states. Even though the cylinder is at the same position, we see different flow fields: a large positive vortex shedding off from the lower surfaces of the cylinder in state 1, while a large negative vortex shedding off from the upper surface in state 2. Fig. 11 (2) and (4) are instantaneous flow fields in the transitional process between the two states.

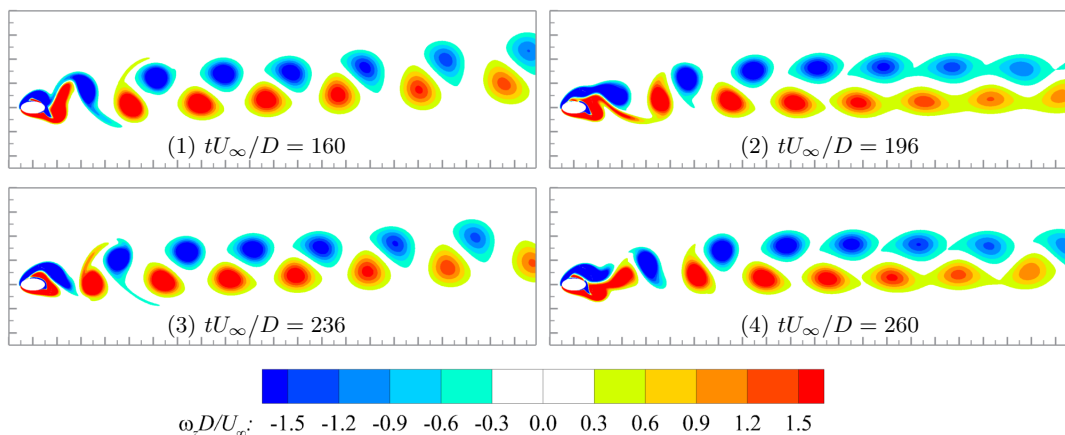


Figure 11. Instantaneous vorticity contours when the elliptic cylinder rotates to  $\phi = 0^\circ$  at  $Re = 200$ .

## IV.B. Reynolds Number 1000

### IV.B.1. Flow Forces

An overall view and a close view of the force coefficients for each cylinder are shown in Fig. 12 and Fig. 13, respectively, where the gray lines are from the 2D simulation and the black lines are from the 3D simulation. It is seen that, there is no obvious difference between the 2D and 3D simulation results for the elliptic cylinder. But differences begin to show up for the triangular cylinder: the lift coefficient from the 3D simulation shows obviously smaller and more consistent oscillation amplitude. This trend continues to the square and the circular cylinders: all force coefficients from the 3D simulation are initially identical to those from the 2D simulation, but soon deviate from the 2D results, showing smaller oscillation magnitudes. These observations indicate that, at this higher Reynolds number, the 2D results are only accurate for a short time (i.e., before transition takes place). For this reason, we mainly focus on the 3D results hereinafter. The decreased oscillation amplitudes in 3D are possibly due to the break down of large coherent vortex structures, which has overall weakened the strength of the vortices. Comparing the 3D results with the  $Re = 200$  results from the previous section, it is interesting to notice a similarity between them: the oscillation amplitudes of forces overall decrease as the number of edges of a cylinder increases, with the circular cylinder having the smallest oscillation amplitudes.

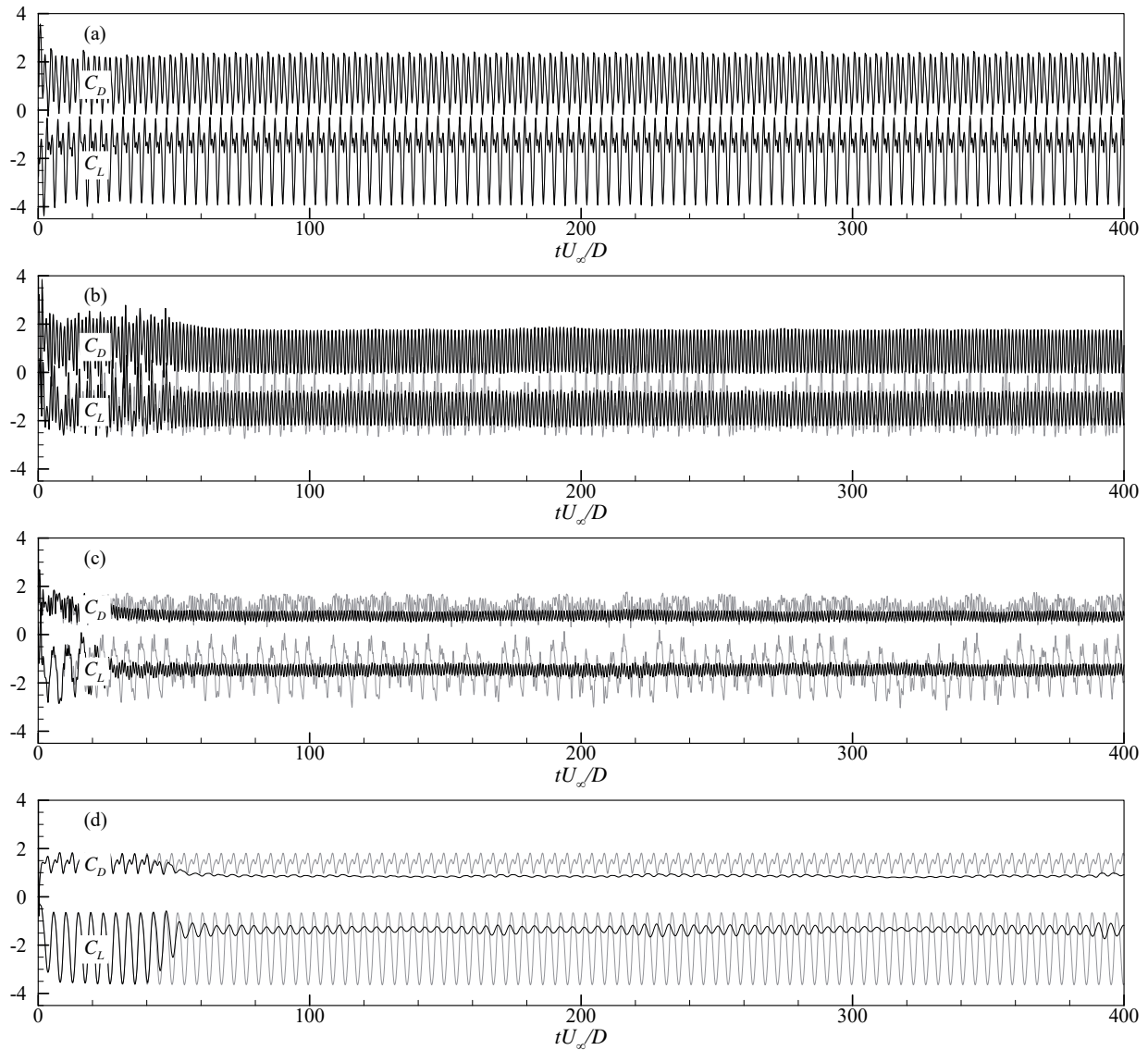


Figure 12. Overall views of  $C_L$  and  $C_D$  at  $Re = 1000$  from 2D (gray) and 3D (black) simulations.

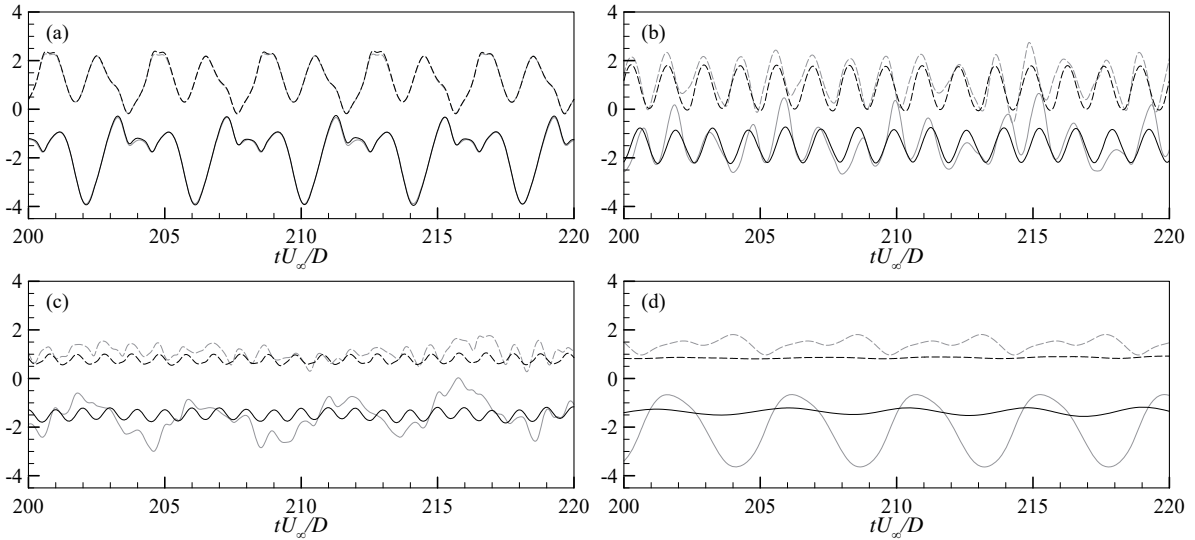


Figure 13. Close views of  $C_L$  (solid) and  $C_D$  (dashed) at  $Re = 1000$  from 2D (gray) and 3D (black) simulations.

Statistics of the lift and drag coefficients, based on data from  $tU_\infty/D = 100$  to 400, are shown in Table 4 and Table 5, respectively. It is seen that almost all the previous conclusions on Table 1 and Table 2 are still valid here. For example, pressure once again contributes much more than friction does to the mean as well as to the unsteady forces. But compared with Table 1 and Table 2, there are several distinctions at this higher Reynolds number. Firstly, we see a further decrease on friction effects for almost all the cylinders. Secondly, all the cylinders except the elliptic one, have smaller lift and drag coefficients. Thirdly, as the number of edges increases,  $\bar{C}_L$ ,  $(C_L)_{rms}$  and  $(C_D)_{rms}$  consistently decrease.

	$\bar{C}_L$	$\bar{C}_{L,p}$	$\bar{C}_{L,f}$	$(C_L)_{rms}$	$(C_{L,p})_{rms}$	$(C_{L,f})_{rms}$	$(C_{L,f})_{rms}:(C_{L,p})_{rms}$
elliptic	-1.738	-1.680 (96.7%)	-0.057 (3.3%)	1.014	1.002	0.027	2.7:100
triangular	-1.503	-1.433 (95.3%)	-0.070 (4.7%)	0.481	0.520	0.042	8.1:100
square	-1.465	-1.400 (95.6%)	-0.065 (4.4%)	0.172	0.161	0.019	11.8:100
circular	-1.367	-1.339 (97.8%)	-0.028 (2.2%)	0.117	0.112	0.005	4.5:100

Table 4. Mean and rms values of the lift coefficients at  $Re = 1000$  from 3D simulation.

	$\bar{C}_D$	$\bar{C}_{D,p}$	$\bar{C}_{D,f}$	$(C_D)_{rms}$	$(C_{D,p})_{rms}$	$(C_{D,f})_{rms}$	$(C_{D,f})_{rms}:(C_{D,p})_{rms}$
elliptic	1.197	1.093 (91.3%)	0.104 ( 8.7%)	0.779	0.773	0.026	3.4:100
triangular	0.872	0.853 (97.8%)	0.020 ( 2.2%)	0.640	0.683	0.046	6.7:100
square	0.756	0.737 (97.5%)	0.020 ( 2.5%)	0.143	0.131	0.021	16.0:100
circular	0.858	0.768 (89.5%)	0.090 (10.5%)	0.036	0.035	0.002	5.7:100

Table 5. Mean and rms values of the drag coefficients at  $Re = 1000$  from 3D simulation.

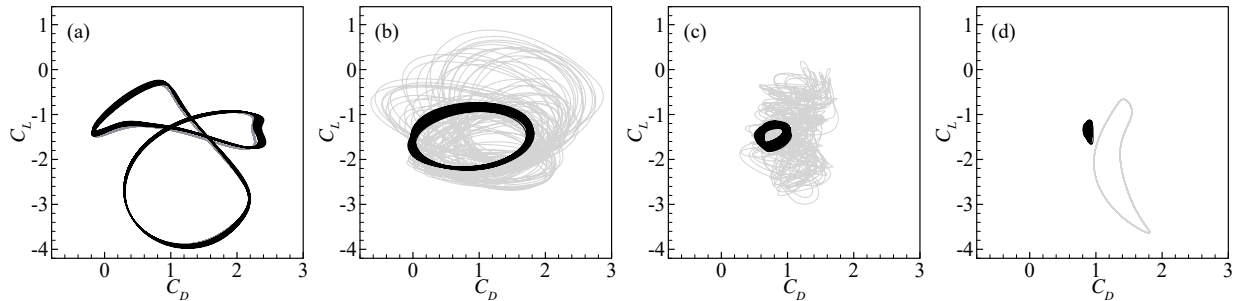


Figure 14. Phase diagrams at  $Re = 1000$  from 2D (gray) and 3D (black) simulations.

The phase diagrams of  $C_L$  and  $C_D$ , covering data from  $tU_\infty/D = 200$  to 300 (i.e., 25 rotation periods), are plotted in Fig. 14 for the 2D and the 3D simulations. As we can see, for all the cylinders except the elliptic one, the 2D simulation over-predicts the forces, resulting in larger diagram shapes than those from the 3D simulation. The 3D results indicate that all the flows are not perfectly periodic at this Reynolds number. Also, the reducing shape size with increasing number of edges indicates smaller oscillation amplitudes.

#### IV.B.2. Flow Frequencies

The spectra of the unsteady force coefficients (based on data from  $tU_\infty/D = 100$  to 400) are shown in Fig. 15. The dominant frequencies are summarized in Table 6. Comparing with Fig. 9 and Table 3, it is seen that increasing the Reynolds number has changed the frequency distributions of the flows. For the elliptic cylinder, the dominant frequency on  $c_L$  has changed from 0.50 to 0.25. Forces on the triangular and the square cylinders have changed from multi-frequency to almost mono-frequency, with the dominant frequencies still being multiples of the rotation frequency though. The dominant frequency for the circular cylinder has gone up from 0.195 to 0.222.

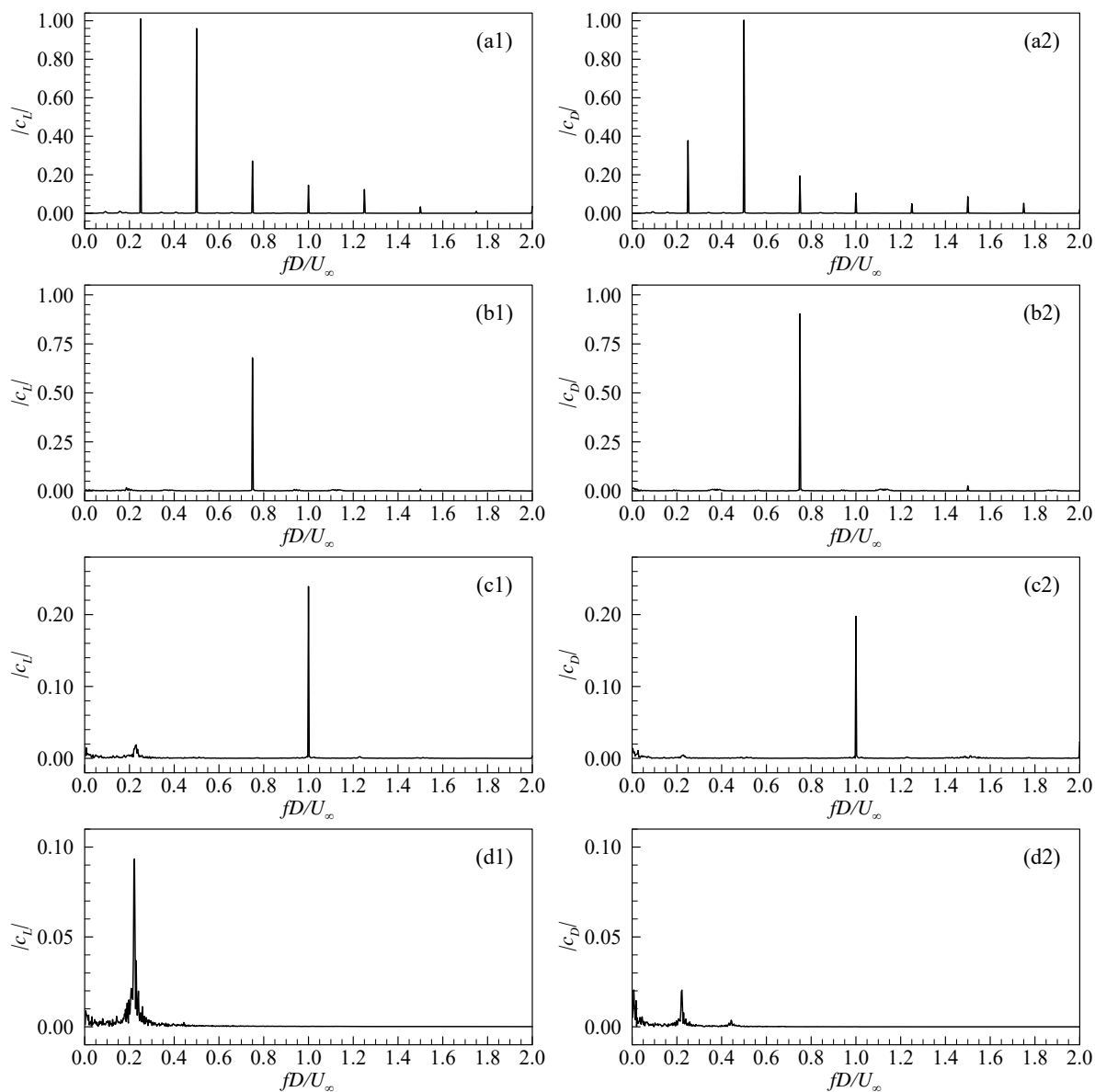


Figure 15. Spectra of the unsteady lift and drag coefficients at  $Re = 1000$  from 3D simulation.

	elliptic	triangular	square	circular
$f_L^*$	0.250	0.750	1.000	0.222
$f_D^*$	0.500	0.750	1.000	0.222

Table 6. Dominant frequencies on the unsteady lift and drag coefficients at  $Re = 1000$  from 3D simulation.

### IV.B.3. Flow Fields

The fully developed flow fields are visualized using isosurfaces of the  $Q$  criterion, and several instantaneous views are plotted in Fig. 16. Overall, all flow fields show abundant vortical structures of various shapes and sizes. A careful review of the results indicates that the flows share similarities and also show distinctions. For example, for all the cylinders, vortices from the top surfaces break down almost immediately, while vortex tubes generated by the lower surfaces are quite strong and stable. The wake of the elliptic cylinder is much more organized and coherent compared with those of the other cylinders — it has a lower row of almost isolated vortex tubes, and an upper row of distorted vortex tubes surrounded by vortex filaments that are connected to the immediate upstream vortex. This “less break-down” wake results in aerodynamic forces that are almost identical to those of the two-dimensional flow as demonstrated by Fig. 12(a) and Fig. 13(a). The sharp edges of the triangular and the square cylinders cause vortices to break down sooner and more complete than the elliptic and the circular cylinders whose surfaces are smooth. This directly leads to smaller and less coherent vortices that are dissipated quicker by viscosity, and in turn a shorter wake than those of the other two cylinders.

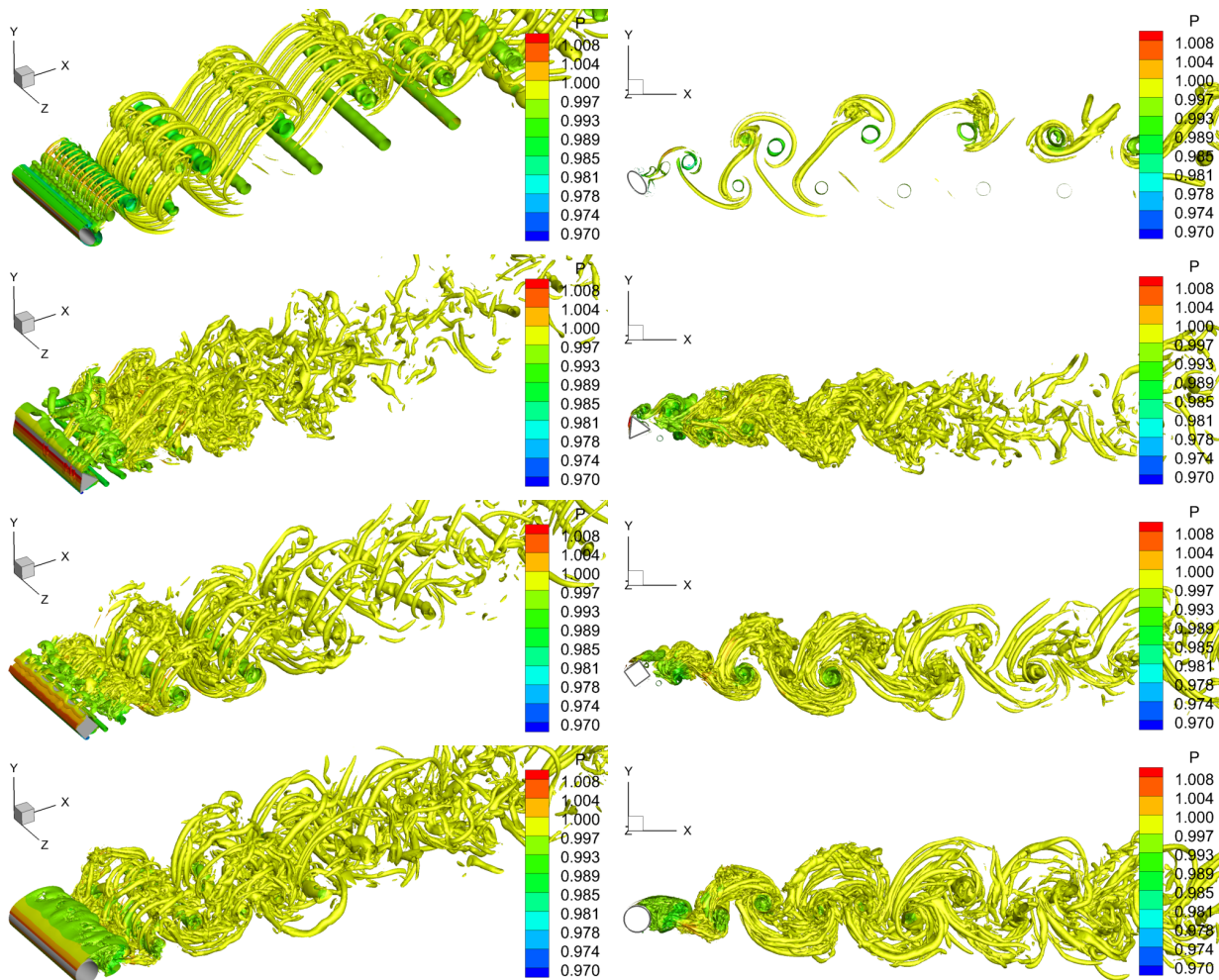


Figure 16. Isosurfaces of  $Q$ -criterion=1 (colored by pressure) at  $Re = 1000$ .

## V. Conclusions

We have successfully applied our high-order sliding-mesh method to the simulation of flow over rotating cylinders of various cross-sectional shapes at a rotation ratio of  $\pi/4$  and two Reynolds numbers of 200 and 1000 in both two- and three-dimension. Three fundamental properties of the flows are investigated: flow forces, frequencies, and structures. We summarize the most interesting findings in what follows.

From flow force analysis, it is found that: (1) All cylinders experience a positive drag and negative lift all the time. (2) The largest mean lift and drag are found on the circular cylinder when the Reynolds number is low, and on the elliptic cylinder when the Reynolds number is high. (3) The elliptic cylinder always shows the largest force oscillations. (4) Pressure, instead of friction, has dominant contribution to both the mean and the unsteady forces in all cases. (5) Overall, as the number of edges increases, a cylinder has smaller force oscillations, and the circular cylinder at the higher Reynolds number experiences almost steady forces.

From frequency analysis, it is found that: (1) The elliptic, triangular, and square cylinders are mostly dominated by the rotations motions. (2) The dominant frequency of the circular cylinder are not multiples of the rotation frequency, and it increases with Reynolds number. (3) Among all the flows, that around the circular cylinder at the lower Reynolds number is found to be the most periodic.

From flow field visualization, it is found that: (1) The flow around the elliptic cylinder at the lower Reynolds number has two stable states. (2) The 2D simulation at the higher Reynolds number is accurate only before transition happens, and it over-predicts forces for the converged flows. (3) At the higher Reynolds number, flow around the elliptic cylinder is the most stable one, and the 2D and 3D simulations give almost identical forces for this flow.

## References

- [1] Zdravkovich, M. M., *Flow around Circular Cylinders Volume 1: Fundamentals*, Oxford University Press, 1997.
- [2] Zdravkovich, M. M., *Flow around Circular Cylinders Volume 2: Applications*, Oxford University Press, 2003.
- [3] Matsui, T., *Flow visualisation studies of vortices*, Survey in Fluid Mechanics, Macmillan, 1982.
- [4] Coutanceau, M., and Menard, C., “Influence of rotation on the near-wake development behind an impulsively started circular cylinder,” *Journal of Fluid Mechanics*, Vol. 158, 1985, pp. 399–446.
- [5] Chew, Y. T., Cheng, M., and Luo, S. C., “A numerical study of flow past a rotating circular cylinder using a hybrid vortex scheme,” *Journal of Fluid Mechanics*, Vol. 299, 1995, pp. 35–71.
- [6] Mittal, S., and Kumar, B., “Flow past a rotating cylinder,” *Journal of Fluid Mechanics*, Vol. 476, 2003, pp. 303–334.
- [7] Chan, A. S., Dewey, P. A., Jameson, A., Liang, C., and Smits, A. J., “Vortex suppression and drag reduction in the wake of counter-rotating cylinders,” *Journal of Fluid Mechanics*, Vol. 679, 2011, pp. 343–382.
- [8] Zhang, B., and Liang, C., “A simple, efficient, and high-order accurate curved sliding-mesh interface approach to spectral difference method on coupled rotating and stationary domains,” *Journal of Computational Physics*, Vol. 295, 2015, pp. 147–160.
- [9] Zhang, B., Liang, C., Yang, J., and Rong, Y., “A 2D parallel high-order sliding and deforming spectral difference method,” *Computers & Fluids*, Vol. 139, 2016, pp. 184–196.
- [10] Zhang, B., and Liang, C., “A high-order sliding-mesh spectral difference solver for simulating unsteady flows around rotating objects,” *31st Symposium on Naval Hydrodynamics*, Monterey, CA, 2016.
- [11] Zhang, B., Qiu, Z., and Liang, C., “A flux reconstruction method with nonuniform sliding-mesh interfaces for simulating rotating flows,” *AIAA paper 2018-1094*, 2018.
- [12] Kopriva, D. A., and Koliass, J. H., “A conservative staggered-grid Chebyshev multidomain method for compressible flows,” *Journal of Computational Physics*, Vol. 125, 1996, pp. 244–261.
- [13] Kopriva, D. A., “A conservative staggered-grid Chebyshev multidomain method for compressible flows. II. A semi-structured method,” *Journal of Computational Physics*, Vol. 128, 1996, pp. 475–488.
- [14] Kopriva, D. A., “A staggered-grid multidomain spectral method for the compressible Navier-Stokes equations,” *Journal of Computational Physics*, Vol. 143, 1998, pp. 125–158.

- [15] Liu, Y., Vinokur, M., and Wang, Z. J., “Spectral difference method for unstructured grids I: Basic formulation,” *Journal of Computational Physics*, Vol. 216, 2006, pp. 780–801.
- [16] Wang, Z. J., Liu, Y., May, G., and Jameson, A., “Spectral difference method for unstructured grids II: Extension to the Euler equations,” *Journal of Scientific Computing*, Vol. 32, 2007, pp. 45–71.
- [17] May, G., and Schöberl, J., “Analysis of a spectral difference scheme with flux interpolation on raviart-thomas elements,” *Aachen Institute for Advanced Study in Computational Engineering Science, Aachen*, 2010.
- [18] Huynh, H. T., “A flux reconstruction approach to high-order schemes including discontinuous Galerkin methods,” *AIAA paper 2007-4079*, 2007.
- [19] Huynh, H. T., “A reconstruction approach to high-order schemes including discontinuous Galerkin for diffusion,” *AIAA paper 2009-403*, 2009.
- [20] Wang, Z. J., and Gao, H., “A unifying lifting collocation penalty formulation including the discontinuous Galerkin, spectral volume/difference methods for conservation laws on mixed grids,” *Journal of Computational Physics*, Vol. 228, 2009, pp. 8161–8186.
- [21] Vincent, P. E., Castonguay, P., and Jameson, A., “A new class of high-order energy stable flux reconstruction schemes,” *Journal of Scientific Computing*, Vol. 47, 2011, pp. 50–72.
- [22] Jameson, A., Vincent, P. E., and Castonguay, P., “On the non-linear stability of flux reconstruction schemes,” *Journal of Scientific Computing*, Vol. 50, No. 2, 2012, pp. 434–445.
- [23] Huynh, H. T., Wang, Z. J., and Vincent, P. E., “High-order methods for computational fluid dynamics: A brief review of compact differential formulations on unstructured grids,” *Computers & Fluids*, Vol. 98, 2014, pp. 209–220.
- [24] Wang, Z. J., and Huynh, H. T., “A review of flux reconstruction or correction procedure via reconstruction method for the Navier-Stokes equations,” *Mechanical Engineering Reviews*, Vol. 3, No. 1, 2016.
- [25] Thomas, P. D., and Lombard, C. K., “Geometric conservation law and its application to flow computations on moving grids,” *AIAA Journal*, Vol. 17, 1979, pp. 1030–1037.
- [26] Rusanov, V. V., “Calculation of interaction of non-steady shock waves with obstacles,” *Journal of Computational and Mathematical Physics USSR*, Vol. 1, 1961, pp. 267–279.
- [27] Kraaijevanger, J. F. B. M., “Contractivity of Runge-Kutta methods,” *BIT Numerical Mathematics*, Vol. 31, No. 3, 1991, pp. 482–528.
- [28] Ruuth, S., “Global optimization of explicit strong-stability-preserving Runge-Kutta methods,” *Mathematics of Computation*, Vol. 75, No. 253, 2006, pp. 183–207.
- [29] Qiu, Z., Zhang, B., Liang, C., and Xu, M., “A high-order solver for simulating vortex-induced vibrations using the sliding-mesh spectral difference method and hybrid grids,” *International Journal for Numerical Methods in Fluids*, Vol. 90, No. 4, 2019, pp. 171–194.
- [30] Lei, C., Cheng, L., and Kavanagh, K., “Spanwise length effects on three-dimensional modelling of flow over a circular cylinder,” *Computer Methods in Applied Mechanics and Engineering*, Vol. 190, No. 22-23, 2001, pp. 2909–2923.
- [31] Maruoka, A., “Finite element analysis for flow around a rotating body using Chimera method,” *International Journal of Computational Fluid Dynamics*, Vol. 17, No. 4, 2003, pp. 289–297.